Chinese Chemical Letters 37 (2026) 111187

Contents lists available at ScienceDirect

Chinese Chemical Letters

journal homepage: www.elsevier.com/locate/cclet

Asymmetric coupling of atop-type and hollow-type adsorbed *CO to boost electrocatalytic CO_2-to-C_2 conversion on high-index Cu_2O crystal planes

Wei Peng[a], Yao Shen[a,b], Xiaolin Yu[c], Chenghang Zheng[d], Xiao Zhang[d], Jingkai Zhao[a], Jiexu Ye[a], Shihan Zhang[a,b,*], Xiang Gao[a,b,d]

[a] College of Environment, Zhejiang University of Technology, Hangzhou 310014, China
[b] Zhejiang Key Laboratory of Clean Energy Conversion and Utilization, Science and Education Integration College of Energy and Carbon Neutralization, Zhejiang University of Technology, Hangzhou 310014, China
[c] State Key Laboratory for Structural Chemistry of Unstable and Stable Species, Beijing National Laboratory for Molecular Sciences, CAS Research/Education Center for Excellence in Molecular Sciences, Institute of Chemistry, Chinese Academy of Sciences, Beijing 100190, China
[d] Carbon Neutrality Research Institute, College of Energy Engineering, Zhejiang University, Hangzhou 310027, China

ARTICLE INFO

Article history:
Received 27 October 2024
Revised 8 February 2025
Accepted 8 April 2025
Available online 8 April 2025

Keywords:
Electrocatalytic conversion
Adsorbed *CO
Asymmetric C-C coupling
Self-selective CO-induced strategy
Cu_2O-based catalysts

ABSTRACT

Cuprous oxide (Cu_2O) is one of the most promising catalysts for electrochemical conversion of CO_2 into value-added C_2 products. The efficiency of CO_2-to-C_2 conversion is highly dependent on the Cu_2O crystal plane orientation and the corresponding adsorbed *CO species. Herein, we constructed high-index crystal planes (311) in Cu_2O (CO–Cu_2O) *via* a facile self-selective CO-induced strategy under a CO atmosphere, which was verified by high-resolution transmission electron microscopy (HR-TEM) and atomic force microscopy (AFM) results. By exploiting the high surface energy of the high index crystal planes, *CO species are stabilized in CO–Cu_2O during CO_2RR, resulting in exceptional catalytic performance for CO_2-to-C_2 products. *In situ* infrared spectroscopy revealed that both atop-type ($*CO_{atop}$) and hollow-type ($*CO_{hollow}$) adsorption of *CO species occurred on the CO–Cu_2O. The asymmetric C–C coupling energy barrier between $*CO_{atop}$ and $*CO_{hollow}$ in (311) crystal plane decreases by 47.8% compared to the symmetric coupling of $*CO_{atop}$ in conventional (100) crystal planes. Consequently, the Faradaic efficiency of C_2 products generated with CO–Cu_2O was increased by as high as 100% compared to that with pristine Cu_2O.

© 2025 Published by Elsevier B.V. on behalf of Chinese Chemical Society and Institute of Materia Medica, Chinese Academy of Medical Sciences.

Carbon dioxide (CO_2) is a major contributor to global warming [1,2], which causes serious environmental issues such as ocean acidification and wildfires [3,4]. Electrocatalytic CO_2 reduction reaction (CO_2RR) driven by renewable energy is a potential approach to reduce CO_2 emissions [5–8]. The conversion of CO_2 into important fuels and chemicals by electrocatalytic reduction with great significance, which is conducive to the development of industrial decarbonization. Although the CO_2RR can produce a variety of products such as carbon monoxide (CO), formic acid, methane (CH_4), ethylene (C_2H_4), ethanol, and acetic acid, it is still extremely difficult to achieve the high efficiency and selectivity towards high value C_2 products with high energy density [9–14]. Cuprous oxide (Cu_2O) is one of the most promising catalysts for electrochemical conversion of CO_2 into value-added C_2 products [15–18]. Among these C_2 products, C_2H_4 is extremely attractive as an important raw material in the chemical industry [19]. We therefore urgently need to develop an optimal catalyst to increase the selectivity of C_2H_4 production. The rate-determining step (RDS) for the formation of C_2H_4 involves C–C coupling between adsorbed *CO or coupling of *CO hydrogenated derivatives [20–22]. However, the symmetric binding of atop-type *CO ($*CO_{atop}$) occurs on conventional low-index crystal planes of Cu_2O due to weak *CO adsorption, leading to high-energy barrier C–C coupling reactions and hindering the CO_2-to-C_2 conversion [23].

By adjusting the crystal planes orientation of Cu_2O, the surface energy and affinity of reaction intermediates can be effectively altered, thereby influencing the adsorption and coupling of *CO species and reduction pathway [24–26]. In particular, the design of high-index crystal planes with significant amounts of atomic steps,

* Corresponding author at: College of Environment, Zhejiang University of Technology, Hangzhou 310014, China.
E-mail address: shihanzhang@zjut.edu.cn (S. Zhang).

https://doi.org/10.1016/j.cclet.2025.111187
1001-8417/© 2025 Published by Elsevier B.V. on behalf of Chinese Chemical Society and Institute of Materia Medica, Chinese Academy of Medical Sciences.

edges, and unsaturated coordinated sites, provides more opportunities for the preparation of catalysts with high activity and selectivity [27]. High-index crystal planes, such as (311) or (522) [28], typically exhibit higher *CO binding energies because of the higher surface energy and coordination saturation [29,30]. This results in the formation of more stable adsorbed *CO species compared to $^*CO_{atop}$ thereby improving the C_2 products selectivity [31]. For instance, Han *et al*. synthesized with a controllable Cu_2O (311) crystal plane and its C_2 selectivity was about 37.5 % at −1.4 V *vs*. RHE, which was doubled compared with 16 % for the low-index crystal planes [27]. The highly chemically active high index crystal plane Cu_2O (311) is energetically favorable to reduce and simultaneous evolve Cu_2O fine grains, which benefits charge transfer and increases the local pH by confining OH^-, resulting in high selectivity towards C_2 products.

A conventional approach to tailoring crystal planes involves the introduction of extrinsic additives, such as surfactants and reductants, during catalyst synthesis [32,33]. However, the removal of residual surfactant requires complex procedures and may result in catalyst poisoning [34]. Although use of a reductant, *e.g.*, $NH_2OH{\cdot}HCl$, can address the adverse effects of residual surfactant and expose the desired crystal planes [35], the design of such synthetic protocols remains complex and requires massive trials. Recently, a self-selective strategy involving the introduction of reactants during catalyst synthesis was proposed [36]. Compared with the introduction of extrinsic additives, the proposed self-selective strategy can address the issues of additive residue and need for massive trials. For example, using CO_2 as an inducer to stabilize CO_2 favored crystal planes during self-selective catalyst preparation, thereby promoting the CO_2RR reaction [36,37]. Inspired by this strategy, we believe that the self-selective CO-favored crystal planes can be induced by introducing CO during the synthesis of Cu_2O. This self-selective strategy tends to stabilize the planes that adsorb *CO intermediates most strongly, since the adsorption of the CO molecules reduces the relative surface energies of these planes. This aims to form other types of with stronger adsorbed *CO species besides atop-type, overcoming the limitations of symmetric coupling based on $^*CO_{atop}$ to promote asymmetric C–C coupling.

Here, we developed a novel Cu_2O electrocatalyst with high-index (311) crystal planes (named CO–Cu_2O) synthesized by a facile self-selective CO-induced strategy using CO as an inducer. *In situ* attenuated total reflection surface-enhanced infrared absorption spectroscopy (ATR-SEIRAS) and density functional theory (DFT) calculations revealed that both atop-type and hollow-type adsorption ($^*CO_{hollow}$) of *CO species occurred on CO–Cu_2O. The asymmetric C–C coupling between $^*CO_{atop}$ and $^*CO_{hollow}$ is kinetically favorable, resulting in a lower energy barrier for CO_2RR compared to the symmetric coupling of $^*CO_{atop}$. Consequently, the Faradaic efficiency of the C_2 products (FE_{C2}) generated with CO–Cu_2O was increased by 100 % than that of pristine Cu_2O.

In typical synthesis, the pristine Cu_2O nanoparticles were synthesized under alkaline conditions using ascorbic acid as a reductant [24], while CO–Cu_2O nanoparticles were prepared following the same procedure under a CO atmosphere. Further details on the experimental section, including materials source and preparation method, can be found in Supporting information. Scanning electron microscopy (SEM) images revealed that the prepared Cu_2O and CO–Cu_2O nanoparticles exhibited cubic structural morphology with a diameter of about 600 nm (Figs. S1 and S2 in Supporting information). Based on the results of high-resolution transmission electron microscopy (HR-TEM) images, the interplanar spacings have been reduced from 0.215 nm in pristine Cu_2O to 0.130 nm in CO–Cu_2O (Figs. 1a and b). This indicates that a significant number of (311) crystal planes appear in CO–Cu_2O through the self-selective CO-induced strategy. Atomic force microscopy (AFM) images (Figs. 1c and d, Fig. S3 in Supporting information) revealed that the roughness of CO–Cu_2O was significantly higher than that of pristine Cu_2O because the (311) crystal planes possessing abundant step- and kink- sites [38]. The line profiles (Figs. 1e and f) demonstrated an increase in the height variation on the CO–Cu_2O surface compared to that on the Cu_2O surface. The average heights of the CO–Cu_2O and Cu_2O surfaces, determined *via* line profile extraction analysis, were approximately 6.11 nm and a mere 0.76 nm, respectively. These particulate edges represented undercoordinated sites associated with crystal microfacets, which are considered to play a crucial role in structure-activity relationship [39,40].

As shown in Fig. S4 (Supporting information), the X-ray diffraction (XRD) spectra demonstrated that the peaks attributed to Cu_2O conformed to those of standard Cu_2O (PDF #99–0041). After self-selective induction, the diffraction peaks of CO–Cu_2O are similar to Cu_2O, confirming that no apparent difference between Cu_2O and CO–Cu_2O catalysts in the crystal structure. Besides, the grazing incidence XRD analysis indicated that the (311)/(100) crystal plane intensity ratio in CO–Cu_2O (0.68) was increased by 51 % compared to that in pristine Cu_2O with only 0.45 (Fig. S5 and Table S1 in Supporting information), indicating the increase of the preferential orientation of the crystal planes after the induction. The X-ray photoelectron spectroscopy (XPS) spectra of Cu_2O and CO–Cu_2O exhibited obvious peaks at 932.1 and 952.0 eV (Figs. S6 and S7 in Supporting information), being attributed to the Cu $2p_{1/2}$ and Cu $2p_{3/2}$ of Cu^+, respectively. Additionally, XPS was employed to assess the differences in the O 1s spectra of various Cu_2O catalysts (Fig. S8 in Supporting information). The O 1s spectra were decomposed into peaks at 529.6 and 531.4 eV, corresponding to surface-absorbed oxygen (O_{ads}) and crystal lattice oxygen species (O_{latt}), respectively. The peak ratio between O_{latt} and O_{ads} served as an indicator of the quantity of surface oxygen vacancies (O_v) [41]. Compared to Cu_2O, CO–Cu_2O enriched with O_v could stabilize Cu^+ and thereby strengthen *CO adsorption to promote C–C coupling [42].

To further elucidate the chemical state and coordination environment of Cu in Cu_2O and CO–Cu_2O at the atomic level, the X-ray near edge spectroscopy (XANES) profiles at the Cu K-edge of the prepared Cu_2O and CO–Cu_2O catalysts were compared with those of commercial Cu foil, Cu_2O, and CuO as reference materials (Fig. 2a). The energy positions of the prepared Cu_2O and CO–Cu_2O catalysts were similar to that of reference Cu_2O, confirming that the valence state of Cu was mainly +1. The peak observed at 1.4 Å (without phase correction) in the *R*-space (k^3-weighted) extended X-ray fine structure (EXAFS) spectra could be attributed to coordination between Cu and O atoms (Fig. 2b). By contrast, the peak at 2.6 Å represented Cu-Cu interactions. Similarly, wavelet transform (WT)-EXAFS was employed to further visualize the coexistence of Cu-O and Cu-Cu coordination in Cu_2O and CO–Cu_2O (Figs. 2c and d). The fitting results (Figs. 2e and f, Fig. S9 in Supporting information) showed that the Cu-Cu coordination number in CO–Cu_2O were about 8.96, which was higher than that of Cu_2O at 8.15 (Table S2 in Supporting information). The CO–Cu_2O shows a higher mean Cu-Cu bond length of approximately 3.05 Å than Cu_2O (2.99 Å), which is due to the tensile strain effect induced by the (311) crystal plane. Notably, the ratio of Cu-O to Cu-Cu coordination strengths in CO–Cu_2O was slightly greater than that in commercial Cu_2O, leading to increased structural disorder and potentially more undercoordinated sites [43].

To determine the effect of adsorbed *CO species on the high-index crystal planes of CO–Cu_2O, *in situ* ATR-SEIRAS was carried out (Figs. 3a and b), and peaks were classified as the corresponding intermediates according to reported studies (Fig. 3c). The spectra were collected in CO_2-saturated 0.5 mol/L $KHCO_3$ solution at different potentials from 0 V to −1.0 V *vs*. RHE. The peak intensity is expressed in terms of absorbance and the positive peak represents product formation. In particular, two peaks appeared at approxi-

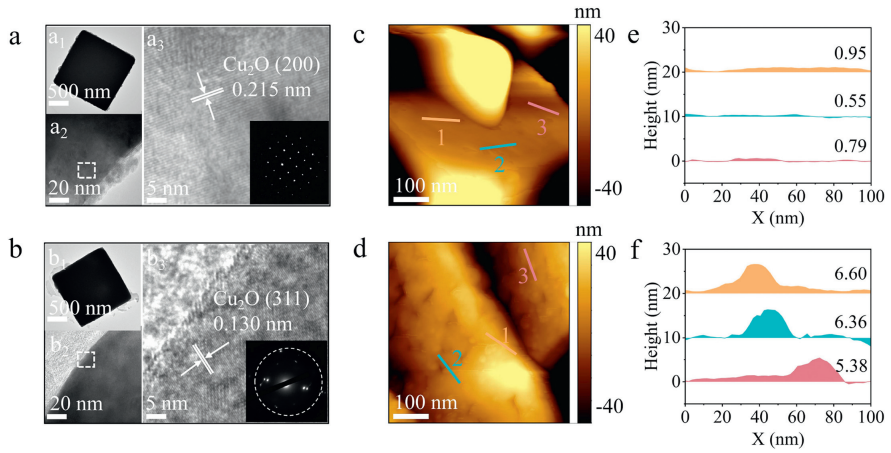


Fig. 1. Morphologies and structural characterization of the prepared catalysts. HR-TEM images of (a) Cu_2O and (b) CO–Cu_2O. AFM images of (c) Cu_2O smooth surface and (d) CO–Cu_2O, showing nanoparticle formation after CO induction. Extracted line profiles for (e) Cu_2O and (f) CO–Cu_2O.

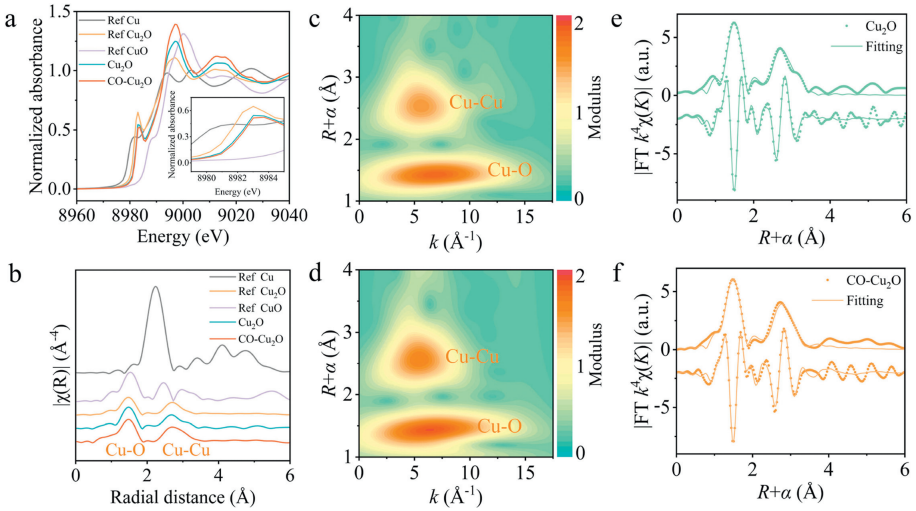


Fig. 2. X-ray fine structure analysis. (a) Normalized Cu K-edge XANES spectra. (b) k^3-weighted Fourier transform EXAFS spectra without phase correction. Cu K-edge WT-EXAFS contour plots of (c) Cu_2O and (d) CO–Cu_2O. Fitting of k space and R space of Cu in (e) Cu_2O and (f) CO–Cu_2O.

mately 2050–1820 cm^{-1} for CO–Cu_2O, which were associated with $*CO_{atop}$ and $*CO_{hollow}$ on the surface, respectively [44]. By comparison, the spectrum of Cu_2O mainly exhibited the $*CO_{atop}$ peak in the same potential region. Two $*CO_{atop}$ peaks were clearly recognized in the spectra of CO–Cu_2O at potentials above −0.4 V *vs.* RHE. The $*CO_{atop}$ peaks could be classified into high-frequency binding *CO (CO–HFB) and low-frequency binding *CO (CO-LFB) [45,46]. Prior research reported that CO-LFB is associated with C–C coupling and C_2H_4 production, while CO–HFB is typically related to the production of gaseous CO [47,48]. Notably, as the potential shifted to more negative values, the red shift observed for the CO stretching bands in the CO–Cu_2O spectra may have been attributed to the Stark effect [49]. This finding suggested an increase in the adsorption of $*CO_{atop}$ on the surface, potentially fostering further protonation or C–C coupling reactions [50]. Hence, we plotted the integrated $*CO_{atop}$ peak area against the applied potentials (Figs. 3d and e).

As the applied potential increased, the integrated area of CO–HFB on the Cu_2O surface decreased, and no CO-LFB appeared within the applied potential range. Meanwhile, CO-LFB was observed on CO–Cu_2O when the applied potential exceeds −0.4 V *vs.* RHE and the integration area reached a maximum at −0.7 V *vs.* RHE. Compared with single CO–HFB on Cu_2O, CO-LFB newly appeared on CO–Cu_2O with a more negative potential. Notably, the absence of CO-LFB signals was detected due to low C–C coupling activity at lower potentials. At higher potentials, the integrated area for CO–Cu_2O dropped owing to *CO consumption for C–C coupling. In addition, new bands emerged on the CO–Cu_2O surface at 1835–1780 cm^{-1} when the applied potential was above −0.4 V *vs.* RHE, corresponding to $*CO_{hollow}$ species [44]. These results suggested that the electronic structure of the catalyst was changed *via* CO induction, which triggered more *CO adsorption configurations. As the potential was further shifted to more negative values, the quantity of adsorbed $*CO_{hollow}$ progressively augmented. Benefiting from the (311) crystal plane in CO–Cu_2O with stronger affinity for *CO, thus CO–Cu_2O catalyst has higher $*CO_{atop}$ and $*CO_{hollow}$ coverage at high overpotentials, further promoting asymmetric C–C coupling. Besides, the peak at 1720 cm^{-1} can be assigned to *CHO (Fig. S10 in Supporting information), which is well accepted as the starting adsorption mode of intermediate for C–C coupling [14,51]. However, no significant *CHO adsorption peak was detected for Cu_2O at all potentials, indicating a high protonation energy barrier affecting subsequent C–C coupling. Meanwhile, an enhanced water (*H-O-H) peak at approximately 1620 cm^{-1} was observed on Cu_2O, which may have led to a blocking effect, facilitating substitution of *H for *CO [52]. Notably, the *H coverage on Cu_2O is opposite to that on CO–Cu_2O, which is associated with higher *CO coverage, resulting in *CO occupying more active sites. In addition, we

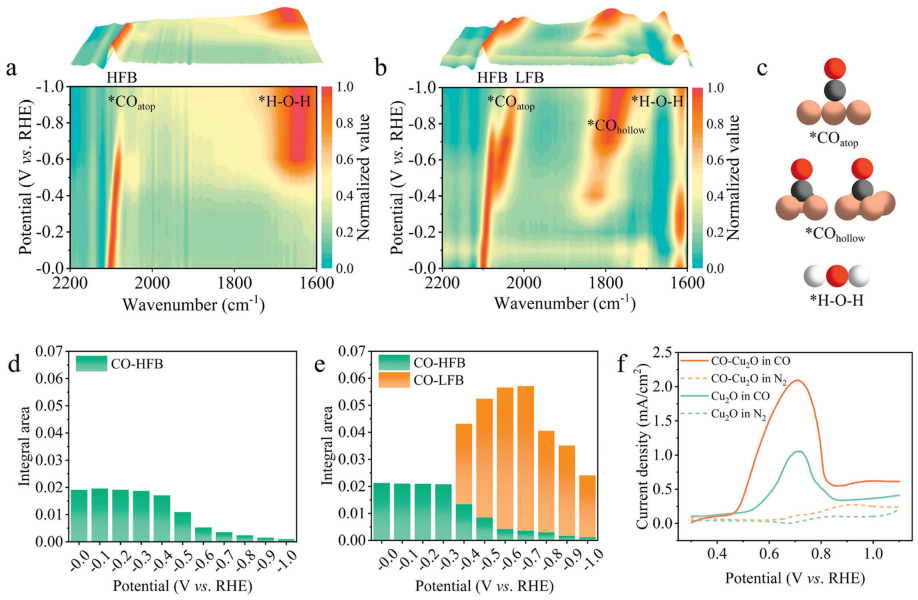


Fig. 3. *In situ* monitoring of adsorbed *CO species. *In situ* ATR-SEIRAS spectra of (a) Cu_2O and (b) CO–Cu_2O during timed current scans from 0 V to −1.0 V *vs.* RHE. (c) The adsorption behavior of species within 2200–1600 cm^{-1} ranges, with Cu, O, C, and H represented by orange, red, gray, and white, respectively. The integrated area of $*CO_{atop}$ for (d) Cu_2O and (e) CO–Cu_2O at various wavenumbers is also shown. The experimental conditions included CO_2-saturated 0.5 mol/L $KHCO_3$ as the electrolyte. Peak positions were determined based on the maximum intensity of the CO stretching band. (f) Electrochemical CO stripping voltammetry curves of Cu_2O and CO–Cu_2O in saturated N_2 or CO atmospheres.

then also investigated the CO adsorption ability of Cu_2O and CO–Cu_2O *via* electrochemical CO stripping voltammetry [53,54]. With the activation process going on, the intensity of oxidic peak corresponding to CO adsorbed on CO–Cu_2O was significantly increased compared to that for Cu_2O (Fig. 3f), indicating stronger CO binding capacity and higher CO coverage that attributed to the increased of electrochemical adsorption of CO [49], which was consistent with the IR spectral analysis. The above results demonstrated that CO–Cu_2O possessed an asymmetric *CO coupling mode and higher *CO coverage than Cu_2O, promoting asymmetric C–C coupling on nearby sites under electrochemical reduction conditions.

To verify the above results, we performed CO_2RR for Cu_2O and CO–Cu_2O. The electrochemical CO_2RR was performed using a flow cell with 0.5 mol/L $KHCO_3$ as electrolyte. The gas chromatography and ^1H nuclear magnetic resonance spectroscopy (^1H NMR) were employed to quantify the products in the gas and liquid phases, respectively. The specific relationships among different products determined from the NMR spectra are presented in Fig. S11 (Supporting information). Linear sweep voltammetry (LSV) images of the Cu_2O and CO–Cu_2O electrodes were acquired in CO_2 or N_2-saturated atmospheres electrolyte (Fig. 4a). Under CO_2 and N_2 atmospheres, Cu_2O catalysts exhibited relatively lower current density (j) values at the same applied potentials than CO–Cu_2O. The results suggested that the increment in high-index crystal planes substantially enhanced the CO_2RR activity of CO–Cu_2O. Figs. 4b and c present the selectivity of CO–Cu_2O under various imposed potentials, where the FE_{C2} (62 %) of CO–Cu_2O was nearly double that of Cu_2O (31 %) at −1.2 V *vs.* RHE. For pristine Cu_2O, the main product was H_2 with nearly 30 % FE, while the C_2H_4 selectivity promoted from 16.2 % to 41.1 % in CO–Cu_2O, whose value was 150 % than pristine Cu_2O. Meanwhile, the partial current density of C_2 products generated with CO–Cu_2O reached 66 mA/cm^2 compared to 25 mA/cm^2 for pristine Cu_2O (Fig. 4d). Additionally, the electrochemical active surface areas (ECSA) of Cu_2O and CO–Cu_2O were measured (Fig. S12 in Supporting information). The ECSA of CO–Cu_2O was 65.8 cm^2, which was larger than that of Cu_2O (50.7 cm^2). This finding indicated that CO–Cu_2O could provide more active sites than Cu_2O. The intrinsic activity of the catalysts was obtained by normalizing the current density to the ECSA [55]. The modified current densities indicated that CO–Cu_2O exhibited greater activity than Cu_2O for C_2 products formation and inhibited H_2 generation (Figs. 4e and f).

As shown in Fig. 4g, CO–Cu_2O achieved a 2.35-fold increase in the FE_{C2}/FE_{C1} ratio at −1.2 V *vs.* RHE compared to pristine Cu_2O. Moreover, CO–Cu_2O exhibited a lower FE_{H2} than pristine Cu_2O at all potentials, and the FE_{C1} of CO–Cu_2O did not significantly increase compared to that of pristine Cu_2O. This suggests that the hydrogen evolution reaction (HER) in CO–Cu_2O was effectively suppressed, and the increased in the amount of C_2 products could be attributed to the inhibition of *H conversion. This is consistent with *in situ* ATR-SEIRAS spectra observations of higher *CO and lower *H coverage, where elevated *CO is involved in the C–C coupling process to form C_2 products. Additionally, the long-term durability performance of CO–Cu_2O catalyst reveal that it maintained a relatively stable current density and C_2H_4 selectivity during the whole operation period (Fig. 4h). Combined with CO_2RR performance, the study findings indicated that $*CO_{hollow}$ became dominant at higher cathodic potential, contributing to asymmetric $*CO_{atop}$ and $*CO_{hollow}$ coupling that enhanced C_2 products formation [50]. As shown in Fig. S13 (Supporting information), electrochemical impedance spectroscopy (EIS) revealed a lower charge transfer resistance (R_{ct}) of CO–Cu_2O at the open circuit potential compared to Cu_2O, which improved the charge transfer kinetics of the developed catalyst compared to pristine Cu_2O. However, CO_2 reduction typically occurs at much more negative applied potentials, and the arcs in the Nyquist diagrams substantially decreased from Cu_2O to CO–Cu_2O, further demonstrating the reduced the transfer resistance of CO–Cu_2O compared to pristine Cu_2O [49]. Hence, it could be concluded that the presence of high-index crystal plane also had an improvement in electron transfer performance to boost the CO_2RR performance.

Stabilizing the Cu^+ content during the CO_2RR process is crucial for generating the corresponding *CO intermediate and final C_2 products [56], whereas presence of Cu^+can promote *CO to *CHO and the adsorption of OH species, causing C_2 intermediates preferably to form the sp^3 hybrid C atom and undergo asymmetric

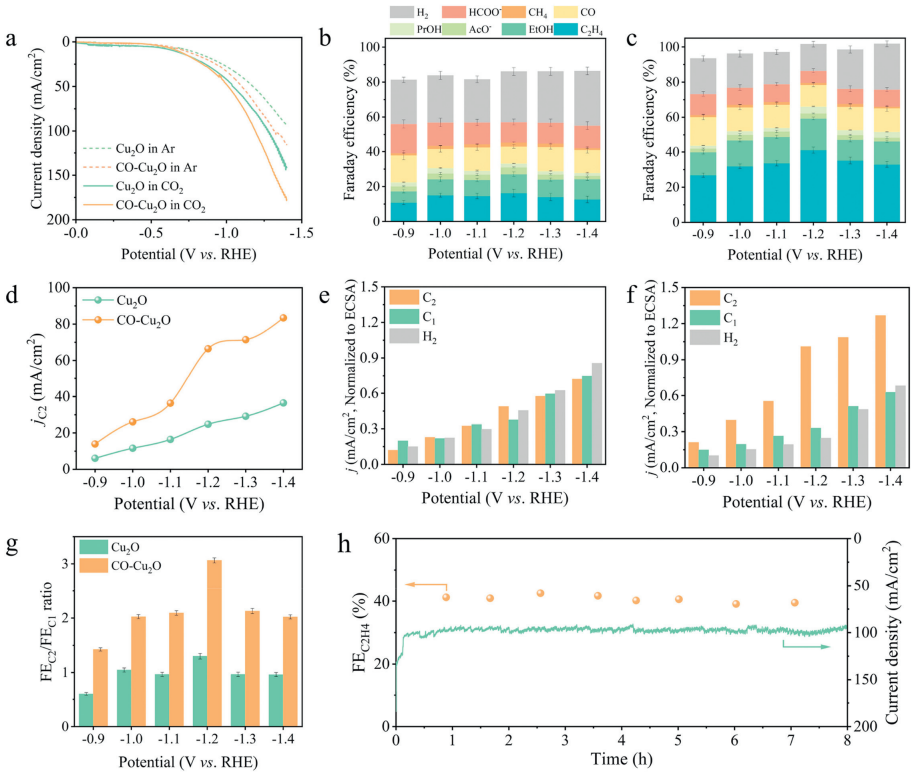


Fig. 4. CO_2-to-C_2 electroreduction performance. (a) Comparison of LSV for CO_2 and Ar-saturated electrolytes. Faradaic efficiency of each product generated with (b) Cu_2O and (c) CO–Cu_2O at various imposed potentials. (d) The partial current density of C_2 products at various potentials over Cu_2O and CO–Cu_2O. ECSA-normalized current density of different products of (e) Cu_2O and (f) CO–Cu_2O. (g) The FE_{C2}/FE_{C1} ratios of Cu_2O and CO–Cu_2O under various imposed potentials. (h) Stability tests of CO–Cu_2O at −1.2 V *vs.* RHE in 0.5 mol/L $KHCO_3$.

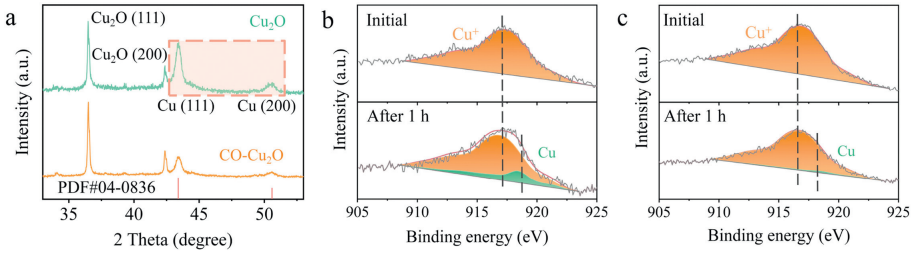


Fig. 5. Cu valence changes in catalysts after CO_2 electroreduction. (a) XRD spectra of Cu_2O and CO–Cu_2O after 1 h of CO_2RR at −1.2 V *vs.* RHE. Cu LMM spectra of (b) Cu_2O and (c) CO–Cu_2O at initial states and those after 1 h of CO_2RR at −1.2 V *vs.* RHE.

hydrogenation, leading to the enhancement of C–C coupling [57]. The SEM images revealed that the surface morphology of CO–Cu_2O after CO_2RR for 1 h at −1.2 V *vs.* RHE had better stability than Cu_2O (Fig. S14 in Supporting information). In addition, the XRD spectra indicated the generation of reduced metal Cu (PDF #04–0836) species on Cu_2O and CO–Cu_2O (Fig. 5a). The peak intensity of Cu (111) and Cu (200) on Cu_2O was significantly higher than that on CO–Cu_2O after the reaction, indicating that more Cu^+ was reduced on Cu_2O. Similarly, the *ex-situ* TEM images and selected area electron diffraction patterns revealed the presence of metallic Cu and Cu^+ in Cu_2O and CO–Cu_2O after the reaction (Fig. S15 in Supporting information), indicating that Cu^+ underwent reduction. Moreover, the stable presence of the (311) plane of CO–Cu_2O is still observed after the reaction, indicating that (311) plane contributes to the formation of stable atomic clusters or structures during electroreduction and that this reconfiguration contributes to the fixation of the Cu^+ valence state. Based on the XRD spectra, the Cu LMM spectra of Cu_2O and CO–Cu_2O after 1 h CO_2RR are examined to show the changing valence state of Cu. The Cu LMM Auger spectra (Figs. 5b and c) clarified that Cu^+ (916.6 eV) and metallic Cu (918.5 eV) species co-existed on the Cu_2O and CO–Cu_2O catalysts. The results indicated that Cu^+ species on CO–Cu_2O remained well stabilized, with only 3 % conversion to metallic Cu, whereas approximately 23 % of Cu^+ in Cu_2O was converted to metallic Cu upon electroreduction. The above results indicate that the CO–Cu_2O catalyst can stabilize the surface morphology and Cu^+ species, which is conducive to maintaining the activity of the electroreduction reaction.

DFT calculations are conducted to verify the possible asymmetric C–C coupling mechanism on Cu_2O (311) crystal plane (Fig. 6a and Fig. S16 in Supporting information). As shown in Fig. 6a, the CO_2 molecule initially adsorbs on the Cu site, undergoing hydrogenation to form the *COOH intermediate. This is then reduced to the *CO intermediate, which combines with protons to yield the *CHO intermediate. Subsequently, the adsorbed *CHO undergoes a similar process to form 2*CHO intermediate on the surface. This 2*CHO intermediate then undergoes dimerization to form the *OHCCHO intermediate, which is finally hydrogenated to produce C_2H_4. Intriguingly, the (311) crystal plane boosts the activation of Cu site and reaches the hollow-type adsorption of *CO, which is

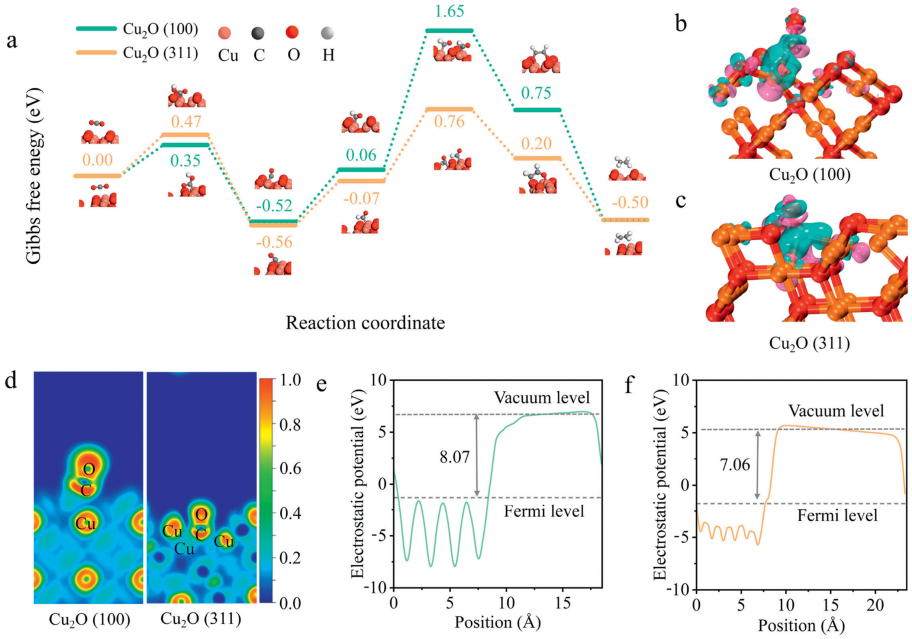


Fig. 6. Mechanistic studies by DFT calculations. (a) The free energy diagrams for CO_2 reduction to different intermediates on the Cu_2O (100) and Cu_2O (311) surfaces at $U = 0$ V. DCD map for the *CO intermediate adsorbed on the (b) Cu_2O (100) and (c) Cu_2O (311) surfaces. (d) ELF of Cu_2O (100) and Cu_2O (311). The WF across the (e) Cu_2O (100) slab and (f) Cu_2O (311) slab vacuum interface.

consistent with the monitoring results from *in situ* spectroscopies. Consequently, the energy barrier of their asymmetric coupling of $*CO_{atop}$ and $*CO_{hollow}$ decreases with 47.8 % compared to the conventional symmetric coupling of $*CO_{atop}$.

The two critical steps in the CO_2RR pathway to C_2H_4 are the hydrogenation of *CO to form the *CHO intermediate and the coupling of *CHO [58]. In the former *CO → *CHO step, the Gibbs free energy change on the Cu_2O (311) surface ($\Delta G = 0.49$ eV) is slightly lower than on the Cu_2O (100) surface ($\Delta G = 0.58$ eV). This suggests that CO–Cu_2O with (311) is more easily protonated, which is consistent with the weaker *CHO that is observed in the infrared spectra. For the *CHO dimerization step, the uphill reaction energy for the formation of 2*CHO from *CHO is an RDS for the entire reaction pathway. In addition, *CO is the pivotal intermediate in the conversion of CO_2 to C_2 products [59,60], with the adsorption energy of *CO playing an important role in their reaction rates [61]. During the activation process, the decomposition of *COOH on Cu_2O (311) has a higher free energy compared to that on Cu_2O (100), indicating that the formation of *CO is more favorable on Cu_2O (311). As shown in Figs. S17 and S18 (Supporting information), the hollow site of the (311) crystal plane exhibited the most robust CO adsorption ($\Delta E = -1.57$ eV), and strong *CO adsorption ensured adequate *CO coverage on its surface [62,63]. In this way, *CO occupied the catalytic active sites on the (311) crystal plane, which strengthened asymmetric C–C coupling and CO_2 to C_2 production.

To better visualize the incorporation of the *CO intermediate with the catalysts, we calculated the differential charge density (DCD) of Cu_2O (100) and Cu_2O (311) crystal planes after *CO adsorption (Figs. 6b and c). Compared with the (100) crystal plane, the charge distributed around the Cu atom on the (311) crystal plane moved more toward the C atom side, indicating enhanced binding energy between *CO and the CO–Cu_2O surface. As shown in the electron localization function (ELF) topographical analysis in Fig. 6d, the (311) crystal plane displayed higher electron delocalization around the formed *CO adsorption sites than that of (100) crystal plane. This suggests that *CO adsorbed on the (311) surface favors the formation of a more stable adsorption configuration, resulting in asymmetric C–C coupling. Work function (WF) can serve as a characteristic quantity to evaluate the catalytic activity [64]. Correspondingly, the detailed WF revealed that the WF value in the (311) crystal plane was lower than that of the (100) crystal plane (Figs. 6e and f). The lower the WF value, the more easily electrons can leave the metal, leading to more efficient electron transfer. To summarize, Cu_2O (311) surface conducive to the electron transfer to the direction of CO_2 electroreduction, thus enhancing the activity and selectivity for the CO_2RR performance.

In summary, the asymmetric coupling of atop-type and hollow-type adsorbed *CO species occurring on the constructed high-index crystal planes was crucial for enhancing the CO_2-to-C_2 conversion. An efficient catalyst CO–Cu_2O with Cu_2O (311) crystal planes was synthesized *via* the facile self-selective CO-induced strategy proposed in this work. The energy barrier of their asymmetric coupling of $*CO_{atop}$ and $*CO_{hollow}$ decreases with 47.8 % compared to the conventional symmetric coupling of $*CO_{atop}$. Benefiting from the asymmetric coupling mechanism, the FE_{C2} generated with CO–Cu_2O was increased by nearly 100 % at −1.2 V *vs.* RHE compared to that with pristine Cu_2O. This study elucidates the mechanism of asymmetric C–C coupling facilitated on high-index crystal planes and offers a method to design efficient catalysts for CO_2-to-C_2 conversion.

Declaration of competing interest

The authors declare that they have no known competing financial interests or personal relationships that could have appeared to influence the work reported in this paper.

CRediT authorship contribution statement

Wei Peng: Writing – original draft, Visualization, Formal analysis. **Yao Shen:** Writing – review & editing, Writing – original draft, Funding acquisition. **Xiaolin Yu:** Software. **Chenghang Zheng:** Data curation. **Xiao Zhang:** Resources. **Jingkai Zhao:** Visualization. **Jiexu Ye:** Resources. **Shihan Zhang:** Writing – review & editing, Writing

– original draft, Funding acquisition. **Xiang Gao:** Software, Funding acquisition, Formal analysis.

Acknowledgments

The authors thankfully acknowledge the financial support from the National Natural Science Foundation of China (Nos. U23A20677, 22022610 and 52400137), "Pioneer" and "Leading Goose" R&D Program of Zhejiang (Nos. 2022C03146 and 2023C03017), China Postdoctoral Science Foundation (No. 2024T170805), and Zhejiang Provincial Natural Science Foundation of China (No. LDT23E06015B06). The authors acknowledge the support of the Research Computing Center in College of Chemical and Biological Engineering at Zhejiang University for assistance with the calculations.

Supplementary materials

Supplementary material associated with this article can be found, in the online version, at doi:10.1016/j.cclet.2025.111187.

References

[1] Z. Liu, Z. Deng, S. Davis, et al., Nat. Rev. Earth Environ. 4 (2023) 205–206.
[2] P. De Luna, C. Hahn, D. Higgins, et al., Science 364 (2019) eaav3506.
[3] K. Alter, J. Jacquemont, J. Claudet, et al., Nat. Commun. 15 (2024) 2885.
[4] C.A. Phillips, B.M. Rogers, M. Elder, et al., Sci. Adv. 8 (2022) eabl7161.
[5] F. Dattila, R.R. Seemakurthi, Y.C. Zhou, et al., Chem. Rev. 122 (2022) 11085–11130.
[6] Y. Zhao, X.L. Zu, R.H. Chen, et al., J. Am. Chem. Soc. 144 (2022) 10446–10454.
[7] C. Du, J.P. Mills, A.G. Yohannes, et al., Nat. Commun. 14 (2023) 6142.
[8] Y. Sun, X. Wang, H. Zhang, et al., ACS Catal. 14 (2024) 1351–1362.
[9] J. Feng, L. Wu, S. Liu, et al., J. Am. Chem. Soc. 145 (2023) 9857–9866.
[10] S. Kuang, M. Li, X. Chen, et al., Chin. Chem. Lett. 34 (2023) 108013.
[11] Y. Sun, J. Xie, Z. Fu, et al., ACS Nano 17 (2023) 13974–13984.
[12] H. Zhang, X. Wang, Y. Sun, et al., Appl. Catal. B 351 (2024) 123992.
[13] C. Sun, J. Hao, B. Wei, et al., Chin. Chem. Lett. 34 (2023) 108520.
[14] X. Chen, A. Xu, D. Wei, et al., Chin. Chem. Lett. 36 (2025) 110175.
[15] H. Yang, Y.W. Hu, J.J. Chen, et al., Adv. Energy Mater. 9 (2019) 1901396.
[16] W.H. Lee, C. Lim, S.Y. Lee, et al., Nano Energy 84 (2021) 105859.
[17] Y. Yao, Y. Zhou, X. Liu, et al., J. Mater. Chem. A 10 (2022) 20914–20923.
[18] Y. Zhou, Y. Yao, R. Zhao, et al., Angew. Chem. Int. Ed. 61 (2022) e202205832.
[19] F.M. Yap, J.Y. Loh, S. Yuan, et al., Adv. Funct. Mater. 35 (2025) 2407605.
[20] W. Deng, P. Zhang, Y. Qiao, et al., Nat. Commun. 15 (2024) 892.
[21] Y. Liang, J. Zhao, Y. Yang, et al., Nat. Commun. 14 (2023) 474.
[22] T. Qin, Y. Qian, F. Zhang, et al., Chin. Chem. Lett. 30 (2019) 314–318.
[23] C. Wang, Z. Lv, Y. Liu, et al., Angew. Chem. Int. Ed. 63 (2024) e202411216.
[24] Y. Gao, Q. Wu, X. Liang, et al., Adv. Sci. 7 (2020) 1902820.
[25] K.D. Yang, W.R. Ko, J.H. Lee, et al., Angew. Chem. Int. Ed. 56 (2017) 796–800.
[26] H. Zhang, C. He, S. Han, et al., Chin. Chem. Lett. 33 (2022) 3641–3649.
[27] C. Han, V. Kundi, Z. Ma, et al., Adv. Funct. Mater. 33 (2023) 2210938.
[28] A. Bagger, W. Ju, A.S. Varela, et al., ACS Catal. 9 (2019) 7894–7899.
[29] J. Rosen, G.S. Hutchings, Q. Lu, et al., ACS Catal. 5 (2015) 4293–4299.
[30] H.G. Yang, C.H. Sun, S.Z. Qiao, et al., Nature 453 (2008) 638–641.
[31] M. Li, S.X. Yu, H.W. Huang, et al., Angew. Chem. Int. Ed. 58 (2019) 9517–9521.
[32] J. Zhao, L.B. Sun, S. Canepa, et al., J. Mater. Chem. A 5 (2017) 11905–11916.
[33] M.J. Siegfried, K.S. Choi, Angew. Chem. Int. Ed. 47 (2008) 368–372.
[34] M.D. Susman, Y. Feldman, A. Vaskevich, et al., ACS Nano 8 (2014) 162–174.
[35] H. Luo, B. Li, J.G. Ma, et al., Angew. Chem. Int. Ed. 61 (2022) e202116736.
[36] H.X. Wang, Z. Liang, M. Tang, et al., Joule 3 (2019) 1927–1936.
[37] H. Wu, Z. Wang, B. Tian, et al., Nanoscale 16 (2024) 3034–3042.
[38] T. Wu, M.Z. Sun, B.L. Huang, Angew. Chem. Int. Ed. 60 (2021) 22996–23001.
[39] D.F. Gao, R.M. Arán-Ais, H.S. Jeon, et al., Nat. Catal. 2 (2019) 198–210.
[40] G.H. Simon, C.S. Kley, B.R. Cuenya, Angew. Chem. Int. Ed. 60 (2021) 2561–2568.
[41] C. Yan, W. Luo, H. Yuan, et al., Appl. Catal. B 308 (2022) 121191.
[42] P. Wang, S. Meng, B. Zhang, et al., J. Am. Chem. Soc. 145 (2023) 26133–26143.
[43] H.P. Xu, D. Rebollar, H.Y. He, et al., Nat. Energy 5 (2020) 623–632.
[44] X. Kong, J. Zhao, J. Ke, et al., Nano Lett. 22 (2022) 3801–3808.
[45] Y. Ou, S.D. Li, F. Wang, et al., Chin. J. Catal. 43 (2022) 2026–2033.
[46] J.L. Yin, Z.Y. Gao, F.Y. Wei, et al., ACS Catal. 12 (2022) 1004–1011.
[47] Y. Lum, J.W. Ager, Nat. Catal. 2 (2019) 86–93.
[48] K.P. Kuhl, E.R. Cave, D.N. Abram, et al., Energy Environ. Sci. 5 (2012) 7050–7059.
[49] Y. Yang, A.B. He, H. Li, et al., ACS Catal. 12 (2022) 12942–12953.
[50] H.Y. An, L.F. Wu, L.D.B. Mandemaker, et al., Angew. Chem. Int. Ed. 60 (2021) 16576–16584.
[51] I.V. Chernyshova, P. Somasundaran, S. Ponnurangam, Proc. Natl. Acad. Sci. U. S. A. 115 (2018) E9261–E9270.
[52] M. Zheng, P.T. Wang, X. Zhi, et al., J. Am. Chem. Soc. 144 (2022) 14936–14944.
[53] W. Sugimoto, K. Aoyama, T. Kawaguchi, et al., J. Electroanal. Chem. 576 (2005) 215–221.
[54] J. Feng, L. Zhang, S. Liu, et al., Nat. Commun. 14 (2023) 4615.
[55] Z. Ji, W. Yuan, S. Zhao, et al., Chem Catal. 3 (2023) 100501.
[56] Z.Z. Wu, F.Y. Gao, M.R. Gao, Energy Environ. Sci. 14 (2021) 1121–1139.
[57] S.C. Lin, C.C. Chang, S.Y. Chiu, et al., Nat. Commun. 11 (2020) 3525.
[58] H.W. Deng, C.Y. Guo, P.H. Shi, et al., ChemCatChem 13 (2021) 4325–4333.
[59] M. Asadi, K. Kim, C. Liu, et al., Science 353 (2016) 467–470.
[60] L. Chen, C. Tang, K. Davey, et al., Chem. Sci. 12 (2021) 8079–8087.
[61] A.J. Garza, A.T. Bell, M. Head-Gordon, ACS Catal. 8 (2018) 1490–1499.
[62] Z.H. Zhao, J.R. Huang, P.Q. Liao, et al., J. Am. Chem. Soc. 145 (2023) 26783–26790.
[63] J. Zhang, C.X. Guo, S.S. Fang, et al., Nat. Commun. 14 (2023) 1298.
[64] M.T. Greiner, L. Chai, M.G. Helander, et al., Adv. Funct. Mater. 22 (2012) 4557–4568.